Research Article | Vol. 31, No. 22 / 23 Oct 2023 / Optics Express 36725
Optics EXPRESS

Q-switched vortex waveguide laser generation based on LNOI thin films with implanted Ag nanoparticles

WENQING SUN,[1] YI LIU,[1] CAROLINA ROMERO,[2] JAVIER R. VÁZQUEZ DE ALDANA,[2] FENG REN,[3] YUECHEN JIA,[1] XIAOLI SUN,[1,4] AND FENG CHEN[1,5]

[1]School of Physics, State Key Laboratory of Crystal Materials, Shandong University, Jinan 250100, China
[2]Grupo de investigación en Aplicaciones del Lásery Fotónica, Universidad de Salamanca, Salamanca 37008, Spain
[3]Department of Physics, Center for Ion Beam Application and Center for Electron Microscopy, Wuhan University, Wuhan 430072, China
[4]xlsun@sdu.edu.cn
[5]drfchen@sdu.edu.cn

Abstract: Lithium-niobate-on-insulator (LNOI) thin films have gained significant attention in integrated photonics due to their exceptional crystal properties and wide range of applications. In this paper, we propose a novel approach to realize a Q-switched vortex waveguide laser by incorporating integrated lithium niobate thin films with embedded silver nanoparticles (Ag:LNOI) as a saturable absorber. The saturable absorption characteristics of Ag:LNOI are investigated using a home-made Z-scan system. Additionally, we integrate Ag:LNOI as a saturable absorber into a Nd:YAG "ear-like" cladding waveguide platform, which is prepared *via* femtosecond laser direct writing. By combining this setup with helical phase plates for phase modulation in the resonator, we successfully achieve a passive Q-switched vortex laser with a high repetition rate and narrow pulse duration in the near-infrared region. This work demonstrates the potential applications of LNOI thin films towards on-chip integration of vortex waveguide laser sources.

1. Introduction

Vortex beams, which possess orbital angular momentum (OAM) [1], are widely used in various fields due to their unique properties that distinct them from ordinary beams. These applications include quantum entanglement [2,3], space optical communication [4–6], optical microscopy [7,8], particle manipulation [9,10], etc. In particular, high-quality vortex pulsed lasers with different pulse durations have significant potential in optical fabrication [11], strong field physics [12], micromanipulation [13], etc. To date, several methods have been developed for generating vortex beams. Vortex beams can be generated by spatially phase modulating Gaussian beams using phase elements outside the resonator, such as spiral phase plates [14–16], *q* plate [17,18], space modulator [19], etc. However, vortex beams generated through out-of-cavity modulation often suffer from instability and poor purity. Introducing elements into the resonator to generate vortex beams has been found to effectively improve efficiency and address previous challenges [20–24]. One effective method for generating intracavity pulse vortex beams is the combination of a saturable absorber with a spiral phase plate, leveraging the nonlinear optical modulation effect of saturable absorption [25]. The spiral phase plate allows for the generation of vortex light by introducing a spiral phase term $\exp(il\varphi)$ into the complex amplitude, which varies the optical path differences for different positions of the incident beam passing through the plate. Additionally, the transmission rate of the absorber can be adjusted by controlling the intensity of the incident light, enabling modulation and control of the light signal.

#503501 https://doi.org/10.1364/OE.503501
Journal © 2023 Received 16 Aug 2023; revised 28 Sep 2023; accepted 3 Oct 2023; published 17 Oct 2023

Optics EXPRESS

In recent years, saturable absorbers, particularly novel low-dimensional nanomaterials, have been widely used in passive Q-switched laser systems [26–28]. However, these saturable absorbers have relatively low damage thresholds, resulting in lower repetition rates and wider laser pulses. For example, using a MoS_2 saturable absorber for modulation, the minimum pulse width of the output pulse is only 203 ns, and the maximum repetition rate is only 1.10 MHz [26]. Similarly, the shortest pulse width modulated by $SnSe_2$ is 129 ns, with a maximum repetition frequency of 2.294 MHz [28]. Moreover, low-dimensional nanomaterials are also more susceptible to environmental factors and prone to oxidation, compromising their stability. Therefore, it is crucial to explore high-quality saturable absorbers for achieving narrow pulse width vortex laser output in the field of photonics.

Lithium niobate ($LiNbO_3$ or LN) crystals are highly promising for a range of photonic applications due to their wide optical transparency and exceptional electro-optic, acousto-optic, and nonlinear properties [29–34]. In particular, lithium-niobate-on-insulator thin films possess the bulk properties of lithium niobate while also offering strong optical constraints, making them ideal for the development of high-performance photonic components such as chip-integrated laser sources [35,36], tunable microring resonator [37], electro-optical modulators [38], and photonic crystal plates [35–48]. However, saturable absorbers based on LNOI have received less attention compared to other passive devices. This is primarily due to its weak light absorption in the visible and near-infrared bands, resulting in a low laser intensity threshold and limiting its nonlinear optical performance.

Taking into account the local surface plasmon resonance (LSPR) effect of metallic nanoparticles (NPs), we propose the incorporation of plasmonic silver (Ag) nanoparticles into LNOI thin films through ion implantation. This results in the formation of an Ag:LNOI structure, aimed at tailoring the nonlinear optical properties of LNOI thin films. By leveraging the LSPR effect of the encapsulated Ag NPs, the saturable absorption properties of Ag:LNOI can be significantly enhanced. We investigate the third-order nonlinear optical response of Ag:LNOI using an open-aperture Z-scan device. The results demonstrate that Ag:LNOI exhibits the excellent saturable absorption behavior in the near-infrared region, which can be attributed to the combined optical nonlinearities of Ag NPs and LN substrates. Additionally, Ag:LNOI has been used as a saturable absorber for generating near-infrared Q-switched vortex waveguide laser systems. The optical waveguide can enhance the optical confinement of the optical field, which can reduce the laser threshold and improve the laser efficiency [49,50], so a solid waveguide platform with a unique "ear-like" circular single-clad optical waveguide written by additional track lines on the side has been employed as a gain medium for generating vortex light [51,52]. Combining the phase modulation of the helical phase plate in the resonator, we successfully realize the Q-switched vortex laser in the near-infrared band with a maximum repetition frequency of 5.75 MHz and the shortest pulse duration of 38 ns. As far as we know, this is the shortest pulse duration ever reported for passive Q-switched vortex lasers using an Ag:LNOI saturable absorber.

2. Ag:LNOI sample characterization

The structure diagram of Ag:LNOI is depicted in Fig. 1(a). The LNOI thin film consists of three distinct layers, forming a sandwich-like structure. The Ag^+ ions are implanted into the LN thin films using the LC22-1C0-01 analytical ion implanter from Wuhan University, with an energy of 160 keV. The Ag^+ ions fluence is set to be 1×10^{17} ions/cm^2. As Ag^+ ions aggregate into nanoparticles within the ion range, the top layer, LN films are divided into two regions: the Ag^+ ion implanted region and the pristine region, as illustrated in Fig. 1(b). To characterize the microstructure of the sample, cross-sectional transmission electron microscopy (TEM) investigation is conducted and provided in the Appendix. The results indicate that the single crystal properties of LN thin films are only disrupted within a depth range of approximately 150 nm from the surface layer, specifically within the ion range.

Optics EXPRESS

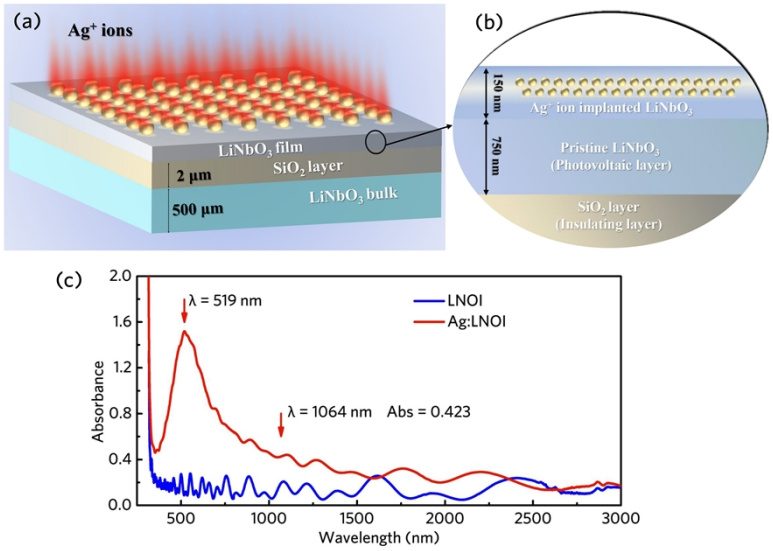

Fig. 1. (a) Schematic diagram of Ag:LNOI prototype structure composed of Ag + ion implanted LN film (900 nm), SiO_2 film (2μm) and LN block substrate (500 μm), (b) schematic diagram of Ag:LNOI cross-section. (c) Linear absorbance spectra of LNOI and Ag:LNOI, respectively.

3. Linear and nonlinear optical properties of Ag:LNOI

The linear absorbance spectra of LNOI and Ag:LNOI are measured by Hitachi U-4100 UV-visible-near-infrared spectrophotometer, respectively. As shown in Fig. 1(c), compared with intrinsic LNOI, the absorption peak is observed at 519 nm for Ag:LNOI sample and shifts towards longer wavelengths. Furthermore, the linear absorption of visible and near-infrared bands experiences a significant enhancement. This enhancement is achieved through the strong LSPR effects. When the incident light interacts with the metallic nanoparticles, collective oscillation of conduction electrons in metallic nanoparticles excites the conduction electrons to higher energy levels, leading to the creation of a localized electromagnetic field around the nanoparticles. This localized field then interacts with the incident light, resulting in a significant enhancement of the electromagnetic field intensity in the vicinity of the nanoparticles. The results show that the introduction of silver nanoparticles not only enhances the linear optical absorption intensity of lithium niobate thin films, but also expands its response bandwidth.

To further verify the saturable absorption characteristics of Ag:LNOI in the 1 μm band, we employ open-aperture Z-scan technology to examine its nonlinear optical response. The experimental setup, as illustrated in Fig. 2(a), involved a mode-locked fiber laser with a pulse duration of 340 fs, repetition rate of 100 kHz, and wavelength of 1030 nm as the excitation laser source. The laser beam waist radius was 30 μm at 1030 nm.

Figure 2(b) illustrates the normalized transmittance variation with the position of the Ag:LNOI sample. It is evident that the peak shape at the focal point (z = 0) is symmetrical, indicating a typical nonlinear absorption curve. This confirms that Ag:LNOI possesses favorable saturation absorption characteristics at 1030 nm. To further determine its saturation fluence and modulation depth, we employ the following equation to perform a nonlinear fit on the acquired data:

$$T = \left(1 - \frac{\Delta R \times I_s}{I_s + \frac{I_0}{1+Z^2/Z_0^2}}\right) / (1 - \Delta R) \tag{1}$$

Optics EXPRESS

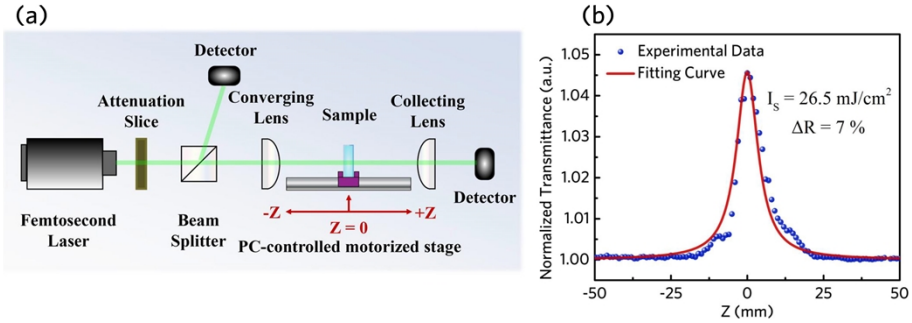

Fig. 2. Open-aperture Z-scan characterization: (a) schematic diagram of Z-scan experimental device, (b) open-aperture Z-scan results.

In the above equation, T represents the normalized transmittance, ΔR stands for the modulation depth of the incident laser beam, I_0 denotes the incident pulse fluence, I_s is the saturation fluence, Z_0 represents the Rayleigh length. With the fitting formula (1), the saturation intensity and modulation depth are determined to be 26.5 mJ/cm^2 and 7.0% at 1030 nm, respectively. These results highlight the significant potential of Ag:LNOI as a saturable absorber in the design of passive Q-switched or mode-locked lasers.

4. Q-switched vortex waveguide laser operation

4.1. Experimental design and setup

Based on the excellent nonlinear absorption characteristics of Ag:LNOI, we use Ag:LNOI as the saturable absorber to realize an efficient passive Q-switched vortex waveguide laser. The schematic diagram of the experimental setup is shown in Fig. 3(a). The Coherent MBR 110, a tunable narrowband continuous-wave Ti:sapphire laser, is employed as the pump source. The pump beam is linearly polarized light with an output wavelength of 808 nm and a radius (1/e^2) of approximately 0.75 mm. A half-wave plate (optical transmittance >98%) is utilized to control its polarization state. To optimize the coupling efficiency and minimize losses, we employ a spherical planoconvex lens with f = 25.6 mm and a 20× microscope objective (NA = 0.40) for internal and external coupling, respectively. In the experiment, a spiral phase plate is employed to mode transform the fundamental mode Gaussian beam into a Laguerre-Gaussian beam within the cavity. Subsequently, the input mirror (coated with an anti-reflection film with a wavelength of 808 nm, light transmittance >99.75%, and coated with a high reflective film with a wavelength of 1064 nm, reflectivity > 99.9%) is applied to the inner coupled end face of the waveguide sample. To improve the integration of the laser, the helical phase plate (topological charge: 1; operating wavelength: 1030 nm; center wavelength bandwidth: ± 35 nm; optical transmittance >99%; clear aperture: 4 mm) not only serves as a phase modulation element but also acts as an output coupler. During Q-switched laser operation, the Ag:LNOI saturable absorber (SA) is inserted into the cavity to modulate the cavity loss, and the optical length of the resonator is approximately 21.8 mm. The laser power is measured using an integrating sphere photodiode power sensor (Thorlabs, S145C), and the spot characteristics of the beam are collected and recorded by a CCD (Charge-coupled Device). Q-switched pulse trains are recorded using an infrared 1 GHz low-noise InGaAs PIN photodetector (New focus, model 1611) and a 25 GHz broadband real-time digital oscilloscope (Tektronix, MSO 71604DX).

We select the high-performance Nd:YAG crystal, which is doped with 1 at. % Nd^{3+} ions. The crystal has been carefully fabricated into an optical waveguide with dimensions of 20 × 10 × 2 mm. as illustrated in Fig. 3(b). All crystal planes have been polished to optical grade. The waveguide structure, written by femtosecond laser direct writing technology, is a circular single-clad optical waveguide with a diameter of 25 µm. Additionally, it features an “ear-like” structure with orbital

Optics EXPRESS

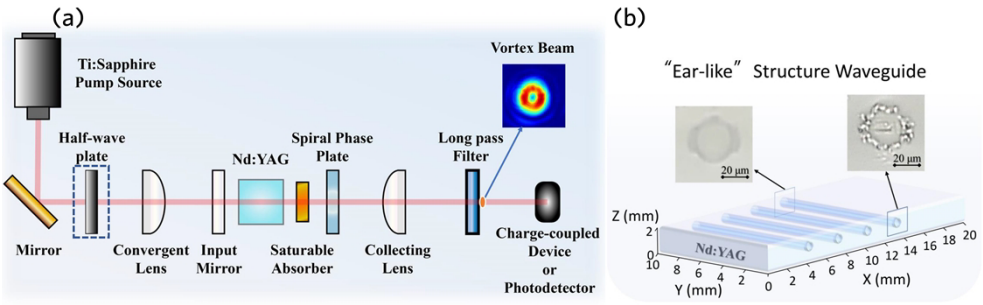

Fig. 3. (a) The schematic diagram of passive Q-switched vortex laser experiment setup. (b) Schematic diagram of Nd:YAG crystals written into the "ear-like" waveguide. Insets are the schematic diagrams of optical microscope cross-section of the 25 μm "ear-like" clad waveguide at the front and back ends of Nd:YAG crystal.

line patterns on both sides. The optical microscope cross section in the inset highlights the waveguide structure at the front and back of the crystal. Due to its reinforced cladding wall, this "ear-like" structure circular single-cladding optical waveguide exhibits a lower laser threshold, higher output power, and improved beam quality compared to ordinary circular single-cladding optical waveguides. Moreover, this unique waveguide structure not only enhances the optical confinement of the light field and mitigates the effects of imperfect boundaries on light guidance but also circumvents the drawback of increasing the overall size of the waveguide structure caused by the introduction of the laser track.

4.2. Results and discussions

To evaluate the performance of waveguide platform, a continuous-wave (CW) vortex waveguide laser without the need for a saturable absorber has been realized, initially. When the laser beam is well collimated, the output laser measured with a CCD is a Laguerre-Gaussian mode vortex beam with a clear doughnut shape, as shown in Fig. 4(b). There is a ring intensity distribution of a dark spot in the center, which is a sign of vortex beam generation. In order to further verify the generation of vortex beams, the topological charge (TC) of vortex beam is measured by using the method called cylindrical lens focusing, and the experimental setup is illustrated in Fig. 4(a). After being focused by the cylindrical lens, the vortex beam with TC of N is focused into N + 1 bright lines, as shown in Fig. 4(c), we can see two clear bright lines, which further proves that a vortex beam with TC of 1 is generated, and its mode is LG_{01}. This is also consistent with the parameters of the spiral phase plate. By analyzing the linear fitting results of the output

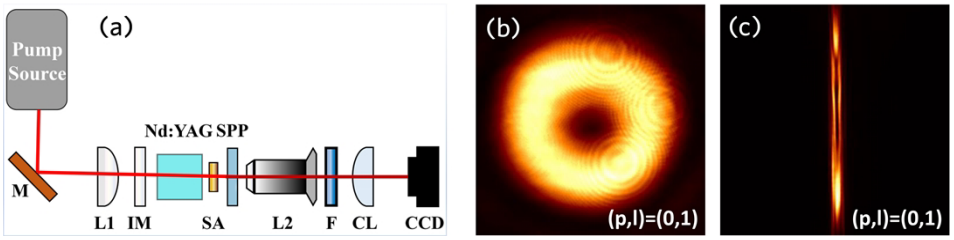

Fig. 4. Measurement of vortex laser and topological charge number. (a) Schematic diagram of measuring experimental setup. L1: convergent lens, IM: input mirror, L2: collecting lens, F: long pass filter, SPP: spiral phase plate, CL: cylindrical lens. (b) Intensity profile of far-field output vortex laser. (c) The intensity profile obtained by focusing the vortex beam with cylindrical lens, p represents the radial index; l represents the angular exponent, which is the topological charge of the vortex beam.

Optics EXPRESS

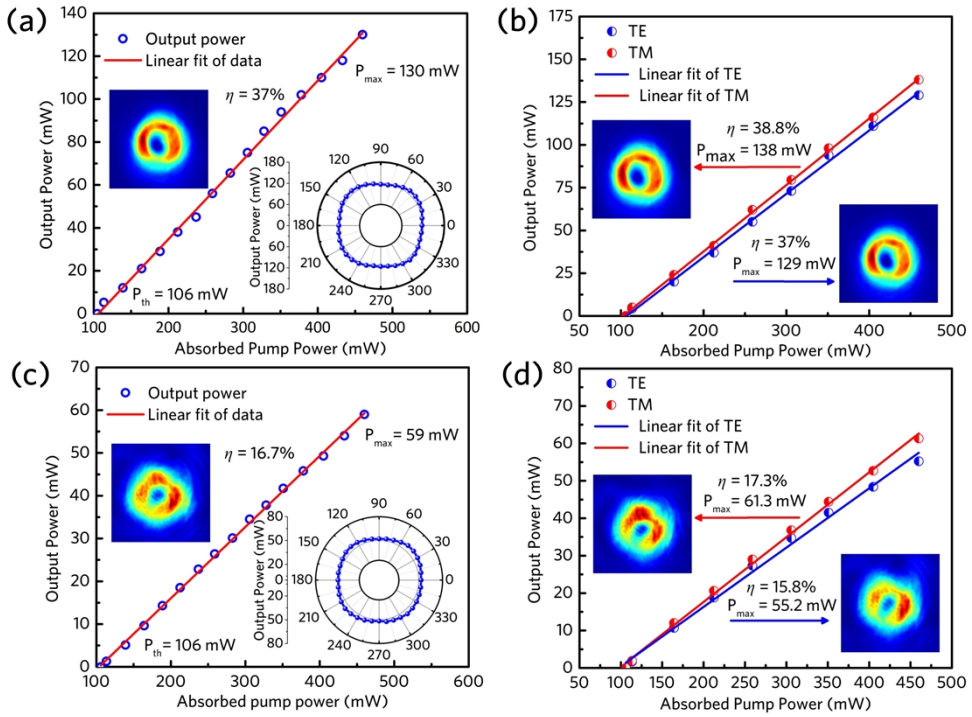

Fig. 5. (a) Output power of CW vortex laser as a function of absorbed pump power. (b) Output power of CW vortex laser as a function of absorbed pump power in the TE/TM polarization. (c) Output power of Ag:LNOI-based passive Q-switched vortex laser as a function of absorbed pump power. (d) Output power of Ag:LNOI-based passive Q-switched vortex laser as a function of absorbed pump power in TE/TM polarization.

power and absorbed pump power of the CW vortex waveguide laser in Fig. 5(a), we find that the oscillation threshold of the CW vortex laser is 106 mW. Additionally, when the absorbed pump power reaches 460 mW, the maximum output power can reach 130 mW with a slope efficiency of 37%. By adjusting the half-wave plate, we can obtain the change in output power for different polarization states, as shown in the inset of Fig. 5(a). The full-angle polarization relation diagram roughly forms a circular shape, indicating that the circular single-cladding optical waveguide with an "ear-like" structure does not exhibit polarization-related laser characteristics. This can be attributed to the fact that the Nd:YAG crystal belongs to the cubic crystal system (a = b = c), and the absorption and emission characteristics in the π and σ directions are essentially the same. The dependence of CW output power on pump power in TE (TM) polarization is depicted in Fig. 5(b). The maximum output power is 129 mW (138 mW) with a slope efficiency of 37% (38.8%), respectively. The attached figures display the Laguerre-Gaussian laser mode images in the TE/TM polarization state, respectively. These results indicate that the "ear-like structure" can enhance the optical confinement along the TM polarization direction while maintaining the laser performance along the TE polarization direction.

By utilizing Ag:LNOI as a saturable absorber, we have successfully achieved a Q-switched vortex laser operating at a wavelength of 1064 nm. As shown in Fig. 5(c), the threshold for the Q-switched vortex waveguide laser is found to be 108 mW, with a maximum output power of 59 mW and a slope efficiency of 16.7%. Additionally, we conducted measurements on the output power of the Q-switched vortex waveguide laser in both TE and TM polarization states, as depicted in Fig. 5(d). It is evident that the output power of the pulsed vortex laser is lower compared to continuous wave operation. This can be attributed to the introduction of a

Optics EXPRESS

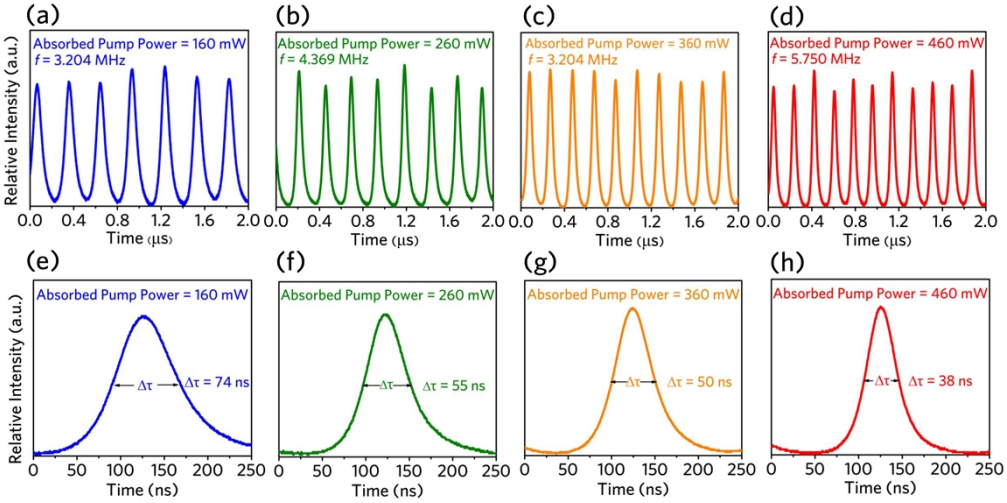

Fig. 6. Recorded pulse train of the Ag:LNOI-based passive Q-switched vortex laser at different absorbed pump power levels (a)160 mW, (b)260 mW, (c)360 mW, (d)460 mW. Recorded monopulse of the Ag:LNOI-based passive Q-switched vortex laser at different absorbed pump power levels (e)160 mW, (f)260 mW, (g)360 mW, (h)460 mW.

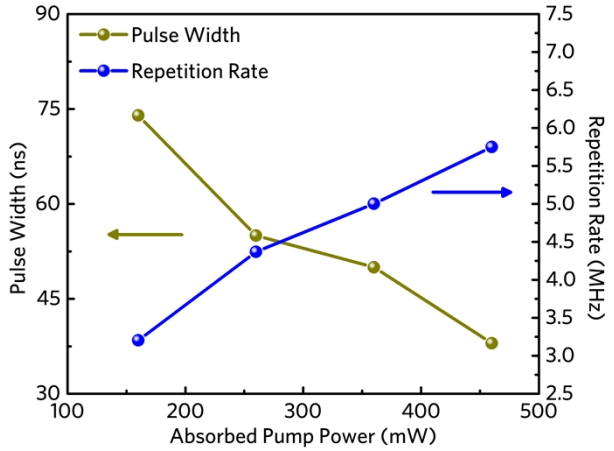

Fig. 7. Pulse width and repetition rate of the Ag:LNOI-based passive Q-switched vortex laser versus absorbed pump power.

saturable absorber and its combination with optical waveguides in transmission mode, which inevitably results in high insertion loss and cavity energy attenuation under the direct field effect. Consequently, the maximum output power and slope efficiency of the pulsed laser are reduced.

The pulse characteristics of Q-switched vortex waveguide based on Ag:LNOI SA at different pump powers are shown in Fig. 6. The pulsed parameters of Q-switched laser based on cladding waveguide with "ear" structure are summarized in Fig. 7. When the absorbed pump power is increased from 160 mW to 460 mW, the repetition rate of the pulse train increases from 3.204 MHz to 5.750 MHz, while the pulse width of a single Q-switched pulse decreases from 74 ns to 38 ns. Q-switched vortex waveguide pulses with a maximum repetition rate of 5.750 MHz and a minimum pulse width of 38 ns were achieved at an absorbed pump power of 460 mW, which is the shortest one ever reported for the passively Q-switched laser by LNOI SA. The stable short pulse output with tens of nanoseconds shows the high quality and stability of the

Optics EXPRESS

Q-switching operation. To the best of our knowledge, this is the first application of Q-switched vortex waveguide laser using Ag:LNOI as an SA based on Nd:YAG waveguide platform. The experimental results showcase the feasibility of utilizing Ag:LNOI, possessing excellent saturation absorption properties, as a saturating absorption material for successfully generating Q-switched vortex waveguide lasers with narrow pulse width and high repetition rate.

5. Conclusions

In summary, we systematically investigate the CW and passive Q-switched laser performance of vortex waveguide laser based on "ear-like" waveguides. By utilizing Ag:LNOI as a saturable absorber on the Nd:YAG "ear-like" circular single-cladding optical waveguide platform, a stable and efficient Q-switched vortex waveguide laser operating has been realized at 1064 nm. The laser exhibits a high repetition rate of 5.750 MHz and a narrow pulse width of 38 ns. It is the significant demonstration in the generation of intracavity Q-switched vortex pulses with high repetition rates and narrow pulse widths. Moreover, this work sheds new light on the development of on-chip integrated vortex laser generation and its potential applications.

Appendix: Ag:LNOI

The cross-sectional transmission electron microscopy image of the Ag:LNOI measured by TEM (FEI Tecnai G2 F20 S-TWIN) is shown in Fig. 8(a). Ag NPs are sphere-like and range in diameter from 2 to 15 nanometers. Moreover, Ag NPs present a Gaussian distribution in the depth range of 150 nm below the surface, with a distribution center at 80 nm, which is basically consistent with our simulation results of ion distribution (Figs. 8(c) and 8(d)). Figure 8(b) shows a high-resolution electron microscope image of the locally amplified Ag nanoparticles. It can be observed that Ag NPs present the excellent crystallization with a lattice of 2.34Å. The above results indicate that the single crystal properties of LN thin films are only disrupted within a depth range of approximately 150 nm from the surface layer, specifically within the ion range.

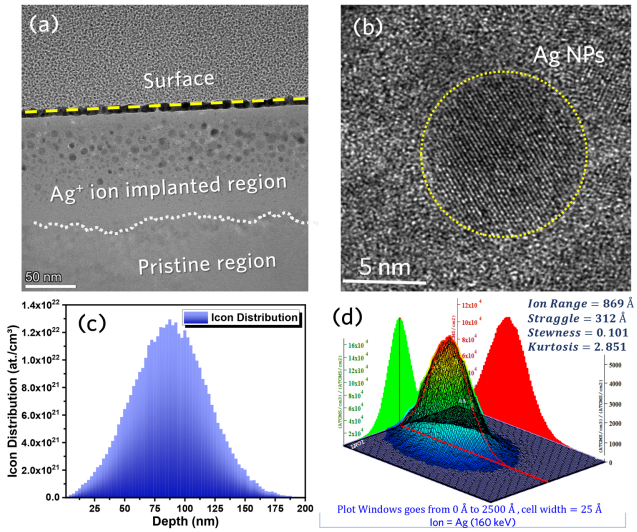

Fig. 8. Morphological characterization of Ag:LNOI: (a) XTEM images in the near surface region, (b) locally amplified HRTEM images characterizing Ag nanoparticles. Ion distribution of Ag^+ ion implanted LN thin films simulated by the software Stopping and Range of Ions in Solid (SRIM): (c) two-dimensional planar distribution diagram, (d) three-dimensional spatial distribution diagram.

Optics EXPRESS

Funding. National Key Research and Development Program of China (2019YFA070500); National Natural Science Foundation of China (12104256, 12134009, 12235009); Natural Science Foundation of Shandong Province (ZR2021QA020); Consejería de Educación, Junta de Castilla y León (SA136P20, SA287P18); Ministerio de Economía y Competitividad (FIS2017-87970R).

Acknowledgments. The authors gratefully acknowledge fruitful discussions with Q. Lu.

Disclosures. The authors declare no conflicts of interest.

Data availability. Data underlying the results presented in this paper are not publicly available at this time but may be obtained from the authors upon reasonable request.

References

1. L. Allen, M. W. Beijersbergen, R. J. C. Spreeuw, and J. P. Woerdman, "Orbital angular momentum of light and the transformation of Laguerre-Gaussian laser modes," Phys. Rev. A **45**(11), 8185–8189 (1992).
2. X. L. Wang, Y. H. Luo, H. L. Huang, M.-C. Chen, Z. E. Su, C. Liu, C. Chen, W. Li, Y. Q. Fang, X. Jiang, J. Zhang, L. Li, N. L. Liu, C. Y. Lu, and J. W. Pan, "18-Qubit Entanglement with Six Photons' Three Degrees of Freedom," Phys. Rev. Lett. **120**(26), 260502 (2018).
3. B. Ndagano, I. Nape, M. A. Cox, C. Rosales-Guzman, and A. Forbes, "Creation and Detection of Vector Vortex Modes for Classical and Quantum Communication," J. Lightwave Technol. **36**(2), 292–301 (2018).
4. J. T. Barreiro, T.-C. Wei, and P. G. Kwiat, "Beating the channel capacity limit for linear photonic superdense coding," Nat. Phys. **4**(4), 282–286 (2008).
5. T. Lei, M. Zhang, Y. Li, P. Jia, G. N. Liu, X. G. Xu, Z. H. Li, C. J. Min, J. Lin, C. Y. Yu, H. B. Niu, and X. C. Yuan, "Massive individual orbital angular momentum channels for multiplexing enabled by Dammann gratings," Light: Sci. Appl. **4**(3), e257 (2015).
6. C. He, Y. J. Shen, and A. Forbes, "Towards higher-dimensional structured light," Light: Sci. Appl. **11**(1), 205 (2022).
7. S. Fürhapter, A. Jesacher, S. Bernet, and M. Ritsch-Marte, "Spiral phase contrast imaging in microscopy," Opt. Express **13**(3), 689 (2005).
8. Y. Kozawa, D. Matsunaga, and S. Sato, "Superresolution imaging via superoscillation focusing of a radially polarized beam," Optica **5**(2), 86 (2018).
9. M. Padgett and R. Bowman, "Tweezers with a twist," Nat. Photonics **5**(6), 343–348 (2011).
10. D. G. Grier, "A revolution in optical manipulation," Nature **424**(6950), 810–816 (2003).
11. L. Yang, D. D. Qian, C. Xin, Z. J. Hu, S. Y. Ji, D. Wu, Y. L. Hu, J. W. Li, W. H. Huang, and J. R. Chu, "Direct laser writing of complex microtubes using femtosecond vortex beams," Appl. Phys. Lett. **110**(22), 221103 (2017).
12. M. Zürch, C. Kern, P. Hansinger, A. Dreischuh, and C. Spielmann, "Strong-field physics with singular light beams," Nat. Phys. **8**(10), 743–746 (2012).
13. L. L. Ran, Z. Y. Guo, and S. L. Qu, "Rotational motions of optically trapped microscopic particles by a vortex femtosecond laser," Chinese Phys. B **21**(10), 104206 (2012).
14. X. X. Liu, J. Y. Zhou, J. C. Xue, and Z. M. Meng, "Coaxial multi-ring optical vortex generation based on compound spiral phase plates," Laser Phys. **32**(3), 035402 (2022).
15. S. N. Khonina, V. V. Kotlyar, M. V. Shinkaryev, V. A. Soifer, and G. V. Uspleniev, "The Phase Rotor Filter," J. Mod. Opt. **39**(5), 1147–1154 (1992).
16. J. T. Xin, K. J. Dai, L. Zhong, Q. X. Na, and C. Q. Gao, "Generation of optical vortices by using spiral phase plates made of polarization dependent devices," Opt. Lett. **39**(7), 1984 (2014).
17. D. L. Li, S. T. Feng, S. P. Nie, J. Ma, and C. J. Yuan, "Scalar and vectorial vortex filtering based on geometric phase modulation with a Q-plate," J. Opt. **21**(6), 065702 (2019).
18. L. Marrucci, E. Karimi, S. Slussarenko, B. Piccirillo, E. Santamato, E. Nagali, and F. Sciarrino, "Spin-to-orbital conversion of the angular momentum of light and its classical and quantum applications," J. Opt. **13**(6), 064001 (2011).
19. Y. J. Shen, Y. Meng, X. Fu, and M. L. Gong, "Wavelength-tunable Hermite–Gaussian modes and an orbital-angular-momentum-tunable vortex beam in a dual-off-axis pumped Yb:CALGO laser," Opt. Lett. **43**(2), 291 (2018).
20. R. Oron, Y. Danziger, N. Davidson, A. A. Friesem, and E. Hasman, "Laser mode discrimination with intra-cavity spiral phase elements," Opt. Commun. **169**(1-6), 115–121 (1999).
21. D. J. Kim and J. W. Kim, "High-power TEM00 and Laguerre–Gaussian mode generation in double resonator configuration," Appl. Phys. B **121**(3), 401–405 (2015).
22. D. J. Kim, J. I. Mackenzie, and J. W. Kim, "Adaptable beam profiles from a dual-cavity Nd:YAG laser," Opt. Lett. **41**(8), 1740 (2016).
23. Y. J. Shen, X. L. Yang, D. Naidoo, X. Fu, and A. Forbes, "Structured ray-wave vector vortex beams in multiple degrees of freedom from a laser," Optica **7**(7), 820 (2020).
24. J. Pan, Y. J. Shen, Z. S. Wan, X. Fu, H. K. Zhang, and Q. Liu, "Index-Tunable Structured-Light Beams from a Laser with an Intracavity Astigmatic Mode Converter," Phys. Rev. Appl. **14**(4), 044048 (2020).
25. Y. B. Wang, Y. J. Shen, Y. Meng, and M. L. Gong, "Generation of 1535-nm Pulsed Vortex Beam in a Diode-Pumped Er,Yb:Glass Microchip Laser," IEEE Photonics Technol. Lett. **30**(10), 891–894 (2018).

Optics EXPRESS

26. C. Cheng, H. L. Liu, Z. Shang, W. J. Nie, Y. Tan, B. D. R. Rabes, Javier R. Vázquez de Aldana, V. De Aldana, D. Jaque, and F. Chen, "Femtosecond laser written waveguides with MoS_2 as satuable absorber for passively Q-switched lasing," Opt. Mater. Express **6**(2), 367 (2016).
27. Y. Tan, Z. N. Guo, L. N. Ma, H. Zhang, S. Akhmadaliev, S. Q. Zhou, and F. Chen, "Q-switched waveguide laser based on two-dimensional semiconducting materials: tungsten disulfide and black phosphorous," Opt. Express **24**(3), 2858 (2016).
28. C. Cheng, Z. Q. Li, N. N. Dong, J. Wang, and F. Chen, "Tin diselenide as a new saturable absorber for generation of laser pulses at 1μm," Opt. Express **25**(6), 6132 (2017).
29. K. Lengyel, Á Péter, L. Kovács, G. Corradi, L. Pálfalvi, J. Hebling, M. Unferdorben, G. Dravecz, I. Hajdara, Z. Szaller, and K. Polgár, "Growth, defect structure, and THz application of stoichiometric lithium niobate," Appl. Phys. Rev. **2**(4), 040601 (2015).
30. Y. C. Jia, L. Wang, and F. Chen, "Ion-cut lithium niobate on insulator technology: Recent advances and perspectives," Appl. Phys. Rev. **8**(1), 011307 (2021).
31. R. S. Weis and T. K. Gaylord, "Lithium niobate: Summary of physical properties and crystal structure," Appl. Phys. A **37**(4), 191–203 (1985).
32. F. Chen and J. R. V. de Aldana, "Optical waveguides in crystalline dielectric materials produced by femtosecond-laser micromachining," Laser Photonics Rev. **8**(2), 251–275 (2014).
33. L. Arizmendi, "Photonic applications of lithium niobate crystals," Phys. Status. Solidi. A **201**(2), 253–283 (2004).
34. Y. F. Kong, F. Bo, W. W. Wang, D. H. Zheng, H. D. Liu, G. Q. Zhang, R. Rupp, and J. J. Xu, "Recent Progress in Lithium Niobate: Optical Damage, Defect Simulation, and On-Chip Devices," Adv. Mater. **32**(3), 1806452 (2020).
35. M. Zhang, B. Buscaino, C. Wang, A. Shams-Ansari, C. Reimer, R. R. Zhu, J. M. Kahn, and M. Lončar, "Broadband electro-optic frequency comb generation in a lithium niobate microring resonator," Nature **568**(7752), 373–377 (2019).
36. S. Dutta, E. A. Goldschmidt, S. Barik, U. Saha, and E. Waks, "Integrated Photonic Platform for Rare-Earth Ions in Thin Film Lithium Niobate," Nano Lett. **20**(1), 741–747 (2020).
37. G. Poberaj, H. Hu, W. Sohler, and P. Günter, "Lithium niobate on insulator (LNOI) for micro-photonic devices," Laser Photonics Rev. **6**(4), 488–503 (2012).
38. S. Yuan, Y. K. Wu, Z. Z. Dang, C. Zeng, X. Z. Qi, G. C. Guo, X. F. Ren, and J. S. Xia, "Strongly Enhanced Second Harmonic Generation in a Thin Film Lithium Niobate Heterostructure Cavity," Phys. Rev. Lett. **127**(15), 153901 (2021).
39. M. Y. Xu, Y. T. Zhu, F. Pittalà, J. Tang, M. He, W. C. Ng, J. Y. Wang, Z. L. Ruan, X. F. Tang, M. Kuschnerov, L. Liu, S. Y. Yu, B. F. Zheng, and X. L. Cai, "Dual-polarization thin-film lithium niobate in-phase quadrature modulators for terabit-per-second transmission," Optica **9**(1), 61 (2022).
40. Y. H. Jiang, X. Han, Y. Y. Li, H. F. Xiao, H. Huang, P. Zhang, A. Dubey, M. Yuan, T. G. Nguyen, A. Boes, Y. T. Li, G. H. Ren, J. Z. Xue, Q. Hao, Y. K. Su, A. Mitchell, and Y. H. Tian, "High-Speed Optical Mode Switch in Lithium Niobate on Insulator," ACS Photonics **10**(7), 2257–2263 (2023).
41. L. Chang, S. T. Liu, and J. E. Bowers, "Integrated optical frequency comb technologies," Nat. Photonics **16**(2), 95–108 (2022).
42. Y. C. Wang, K. D. Jöns, and Z. P. Sun, "Integrated photon-pair sources with nonlinear optics," Appl. Phys. Rev. **8**(1), 011314 (2021).
43. D. Zhu, L. B. Shao, M. J. Yu, R. Cheng, B. Desiatov, C. J. Xin, Y. W. Hu, J. Holzgrafe, S. Ghosh, A. Shams-Ansari, E. Puma, N. Sinclair, C. Reimer, M. Zhang, and M. Lončar, "Integrated photonics on thin-film lithium niobate," Adv. Opt. Photonics **13**(2), 242 (2021).
44. A. A. Sayem, R. S. Cheng, S. H. Wang, and H. X. Tang, "Lithium-niobate-on-insulator waveguide-integrated superconducting nanowire single-photon detectors," Appl. Phys. Rev. **116**(15), 151102 (2020).
45. B. C. Pan, H. X. Liu, Y. S. Huang, Z. J. Yu, H. Li, Y. C. Shi, L. Liu, and D. X. Dai, "Perspective on lithium-niobate-on-insulator photonics utilizing the electro-optic and acousto-optic effects," ACS Photonics **10**, 2078 (2023).
46. F. Sulser, G. Poberaj, M. Koechlin, and P. Günter, "Photonic crystal structures in ion-sliced lithium niobate thin films," Opt. Express **17**(22), 20291 (2009).
47. L. Chang, Y. F. Li, N. Volet, L. Wang, J. Peters, and J. E. Bowers, "Thin film wavelength converters for photonic integrated circuits," Optica **3**(5), 531 (2016).
48. A. Bartasyte, S. Margueron, T. Baron, S. Oliveri, and P. Boulet, "Toward High-Quality Epitaxial LiNbO and LiTaO Thin Films for Acoustic and Optical Applications," Adv. Mater. Interfaces **4**(8), 1600998 (2017).
49. Y. Meng, Y. Z. Chen, L. H. Lu, Y. M. Ding, A. Cusano, J. A. Fan, Q. M. Hu, K. Y. Wang, Z. W. Xie, Z. T. Liu, Y. M. Yang, Q. Liu, M. L. Gong, Q. Xiao, S. L. Sun, M. M. Zhang, X. C. Yuan, and X. J. Ni, "Optical meta-waveguides for integrated photonics and beyond," Light: Sci. Appl. **10**(1), 235 (2021).
50. Y. Meng, Z. T. Liu, Z. W. Xie, R. D. Wang, T. C. Qi, F. T. Hu, H. Kim, Q. R. Xiao, X. Fu, Q. Wu, S.-H. Bae, M. L. Gong, and X. C. Yuan, "Versatile on-chip light coupling and (de)multiplexing from arbitrary polarizations to controlled waveguide modes using an integrated dielectric metasurface," Photonics Res. **8**(4), 564 (2020).
51. A. Okhrimchuk, V. Mezentsev, A. Shestakov, and I. Bennion, "Low loss depressed cladding waveguide inscribed in YAG:Nd single crystal by femtosecond laser pulses," Opt. Express **20**(4), 3832 (2012).

Optics EXPRESS

52. X. L. Sun, S. Sun, C. Romero, Javier R. Vázquez de Aldana, V. de Aldana, F. Q. Liu, Y. C. Jia, and F. Chen, "Femtosecond laser direct writing of depressed cladding waveguides in Nd:YAG with 'ear-like' structures: fabrication and laser generation," Opt. Express **29**(3), 4296 (2021).